

Theoretical Studies of Convectively Forced Mesoscale Flows in Three Dimensions. Part I: Uniform Basic-State Flow

Ji-YOUNG HAN AND JONG-JIN BAIK

School of Earth and Environmental Sciences, Seoul National University, Seoul, South Korea

(Manuscript received 4 August 2008, in final form 22 September 2008)

ABSTRACT

Convectively forced mesoscale flows in three dimensions are theoretically investigated by examining the transient response of a stably stratified atmosphere to convective heating. Solutions for the equations governing small-amplitude perturbations in a uniform basic-state wind with specified convective heating are analytically obtained using the Green function method. In the surface pulse heating case, it is explicitly shown that the vertical displacement at the center of the 3D steady heating decreases as fast as t^{-1} for large t . Hence, unlike in two dimensions, the steady state is approached in three dimensions. In the finite-depth steady heating case, the perturbation vertical velocity field in the stationary mode shows a main updraft region extending over the heating layer and V-shaped upward and downward motions above and below the heating layer. Including the third dimension results in a stronger updraft at an early stage, a weaker compensating downward motion, and a weaker stationary gravity wave field in a quasi-steady state than in the case of two dimensions. An examination of flow response fields for various vertical structures of convective heating indicates that stationary gravity waves above the main updraft region become strong in intensity as the height of the maximum convective heating increases. In response to the transient heating, a main updraft region extending over the heating layer no longer appears at a dissipation stage of deep convection. Instead, alternating regions of upward and downward motion with an upstream phase tilt appear.

1. Introduction

Gravity waves generated in a stably stratified atmosphere play important roles in initiating moist convection, organizing mesoscale circulation itself, maintaining observed middle atmosphere circulation, and so on (e.g., Stobie et al. 1983; Pandya and Durran 1996; Song et al. 2007). Two important sources of atmospheric gravity waves are mechanical forcing, such as topography, and thermal forcing, such as convective heating. Theoretical studies of thermally forced gravity waves have progressed less than those of topographically forced gravity waves because of mathematical complications. In this study, gravity waves forced by convective heating are examined theoretically.

The problem of thermally forced mesoscale flows can be theoretically investigated by considering the response of a stably stratified atmosphere to specified thermal

forcing. Two-dimensional (2D), steady-state studies in a uniform flow with application to urban heat island (Olfe and Lee 1971) and orographic rain (Smith and Lin 1982) problems show that the typical response to localized heating is a downward displacement near a heat source for flows with large Froude number. This negative phase relationship between heating and vertical displacement was explained in a 2D transient study by Lin and Smith (1986). They showed that as a steady state is approached, a region of positive displacement drifting downstream appears, whereas a region of negative displacement develops in the vicinity of a stationary heat source. By investigating the airstream over a three-dimensional (3D) elevated heat source with application to the dynamics of V-shaped clouds, Lin (1986) indicated that a low-level upward motion is produced over an isolated heat source with a wide range of basic-state wind speeds. In a study of urban heat island-induced circulation and convection in three dimensions, Han and Baik (2008) examined a 3D transient response of a stably stratified uniform flow to prescribed low-level heating and highlighted a universal role that the urban heat island plays in precipitation enhancement observed downwind of urban areas.

Corresponding author address: Jong-Jin Baik, School of Earth and Environmental Sciences, Seoul National University, Seoul 151-742, South Korea.
E-mail: jjbaik@snu.ac.kr

In steady-state (e.g., Lin 1987; Lin and Li 1988) and transient (e.g., Baik et al. 1999a,b) studies considering shear flow with a critical level, it is shown that the flow response is strongly dependent on the Richardson number and heating depth and that as gravity waves pass through a critical level, most of wave energy is absorbed there.

For mathematical simplification, most of the linear studies of thermally forced gravity waves are confined to two dimensions. However, as pointed out by Bretherton (1988), the characteristics of gravity waves in three dimensions are different from those in two dimensions. Even though some studies dealt with a 3D problem, they either obtained solutions in wavenumber space, which were numerically inverted to physical space using a fast Fourier transform (FFT) algorithm (Lin 1986; Lin and Li 1988), or they examined the flow response to low-level heating that represents an urban heat island (Han and Baik 2008).

In this study, we solve a 3D transient problem in a uniform flow with elevated heating, obtain analytic solutions in physical space, and try to understand the 3D transient dynamics of convectively forced mesoscale flows. In section 2, governing equations and solutions are given. In section 3, analysis results of the solutions are presented and discussed. We focus on 1) the characteristics of stationary and moving modes forced by deep convective heating, 2) dynamical differences between convectively forced flows in two and three dimensions, 3) the sensitivity of convectively forced flows to the vertical structure of convective heating, and 4) the effects of transient convective heating on convectively forced flows. A summary and conclusions follow in section 4.

2. Governing equations and solutions

In a 3D, time-dependent, hydrostatic, nonrotating, inviscid, Boussinesq airflow system, the equations governing small-amplitude perturbations with diabatic forcing q can be written as

$$\frac{\partial u}{\partial t} + U \frac{\partial u}{\partial x} + V \frac{\partial u}{\partial y} = -\frac{\partial \pi}{\partial x}, \quad (1)$$

$$\frac{\partial v}{\partial t} + U \frac{\partial v}{\partial x} + V \frac{\partial v}{\partial y} = -\frac{\partial \pi}{\partial y}, \quad (2)$$

$$\frac{\partial \pi}{\partial z} = b, \quad (3)$$

$$\frac{\partial b}{\partial t} + U \frac{\partial b}{\partial x} + V \frac{\partial b}{\partial y} + N^2 w = \frac{g}{c_p T_0} q, \quad (4)$$

$$\frac{\partial u}{\partial x} + \frac{\partial v}{\partial y} + \frac{\partial w}{\partial z} = 0, \quad (5)$$

where x - and y -directional basic-state horizontal wind speeds U and V and buoyancy frequency N are taken to be constant with height. Here, u , v , and w are x -, y -, and z -directional perturbation velocities, respectively; π is the perturbation kinematic pressure; b is the perturbation buoyancy; g is the gravitational acceleration; c_p is the specific heat of air at constant pressure; and T_0 is the reference temperature.

The basic strategy for solving the above equations is to use the Green function method. That is, we first obtain the solution to the surface pulse forcing, which is given by

$$q(x, y, z, t) = q_0 \frac{1}{[(x/a_x)^2 + (y/a_y)^2 + 1]^{3/2}} \delta(z - h) \delta(t), \quad (6)$$

where q_0 is the amplitude of the thermal forcing, a_x and a_y determine the respective x - and y -directional horizontal sizes of the thermal forcing, δ is the Dirac delta function, and h is the height at which the surface forcing is applied. Then, the solution to the finite-depth steady or transient forcing, which is regarded as representing latent heating due to cumulus convection, is obtained by integrating the solution to the surface pulse forcing with respect to the forcing level and time.

Equations (1)–(5) can be combined to give a single equation for the perturbation vertical velocity:

$$\begin{aligned} & \left(\frac{\partial}{\partial t} + U \frac{\partial}{\partial x} + V \frac{\partial}{\partial y} \right)^2 \frac{\partial^2 w}{\partial z^2} + N^2 \left(\frac{\partial^2 w}{\partial x^2} + \frac{\partial^2 w}{\partial y^2} \right) \\ & = \frac{g}{c_p T_0} \left(\frac{\partial^2 q}{\partial x^2} + \frac{\partial^2 q}{\partial y^2} \right). \end{aligned} \quad (7)$$

Upon (7), we perform the double Fourier transform in x ($\rightarrow k$) and y ($\rightarrow l$) and the Laplace transform in t ($\rightarrow s$). Then, (7) becomes

$$\frac{d^2 \hat{w}}{dz^2} + N^2 \lambda^2 \hat{w} = \frac{g}{c_p T_0} \lambda^2 \hat{q}, \quad \text{where} \quad (8)$$

$$\lambda = \frac{iK}{s + ikU + ilV}, \quad K = \sqrt{k^2 + l^2},$$

$$\hat{q} = q_0 \frac{a_x a_y}{2\pi} e^{-\sqrt{k^2 a_x^2 + l^2 a_y^2}} \delta(z - h).$$

Equation (8) has the general solution

$$\hat{w}_1(k, l, z, s) = A_1(k, l, s) e^{iN\lambda z} + B_1(k, l, s) e^{-iN\lambda z} \quad \text{for } 0 \leq z \leq h, \quad (9a)$$

$$\hat{w}_2(k, l, z, s) = A_2(k, l, s) e^{iN\lambda z} + B_2(k, l, s) e^{-iN\lambda z} \quad \text{for } z > h. \quad (9b)$$

Applying a flat bottom boundary condition [$\hat{w}_1(k, l, z, s) = 0$ at $z = 0$], an upper radiation condition [$B_2(k, l, s) = 0$], and two interface conditions given by

$$\frac{d\hat{w}_2}{dz} - \frac{d\hat{w}_1}{dz} = \frac{gq_0 a_x a_y}{2\pi c_p T_0} \lambda^2 e^{-\sqrt{k^2 a_x^2 + l^2 a_y^2}} \quad \text{at } z = h \quad \text{and} \quad (10a)$$

$$\hat{w}_2 - \hat{w}_1 = 0 \quad \text{at } z = h \quad (10b)$$

enables us to obtain the four unknown coefficients $A_1(k, l, s)$, $B_1(k, l, s)$, $A_2(k, l, s)$, and $B_2(k, l, s)$. Then, the solution in transformed space becomes

$$\hat{w}_1(k, l, z, s) = iC\lambda e^{-\sqrt{k^2 a_x^2 + l^2 a_y^2}} [e^{iN\lambda(z+h)} - e^{-iN\lambda(z-h)}] \quad \text{for } 0 \leq z \leq h, \quad (11a)$$

$$\hat{w}_2(k, l, z, s) = iC\lambda e^{-\sqrt{k^2 a_x^2 + l^2 a_y^2}} [e^{iN\lambda(z+h)} - e^{iN\lambda(z-h)}] \quad \text{for } z > h, \quad (11b)$$

where

$$C = \frac{gq_0 a_x a_y}{4\pi c_p T_0 N}.$$

The first terms in square brackets of (11a) and (11b) represent upward-propagating gravity waves through reflection at the bottom boundary. The second terms in square brackets of (11a) and (11b) represent downward- and upward-propagating gravity waves, respectively, which come directly from the thermal forcing. We can obtain the solution in physical space by performing the inverse Laplace transform and the inverse double Fourier transform upon (11a) and (11b). Some details are given in appendix A.

3. Results and discussion

a. Surface pulse heating case

Figure 1 shows the time evolution of the perturbation vertical velocity field along $y = 0$ when the surface pulse heating is applied at $z = 1$ km. The specified parameter values in this and the following figures are $U = 10 \text{ m s}^{-1}$, $V = 0 \text{ m s}^{-1}$, $N = 0.01 \text{ s}^{-1}$, $T_0 = 273 \text{ K}$, and $a_x = a_y = 10 \text{ km}$ (Table 1). In Fig. 1, q_0 is 2 J m kg^{-1} . In response to the thermal forcing that is impulsively applied at $t = 0 \text{ s}$, the initial field shows an upward motion near the initial heating center. The upward motion extends in the vertical and has its maximum value at the height where the surface heating is applied. There exists a very weak compensating downward motion over a large region enclosing the upward motion (Fig. 1a). At

$t = 600 \text{ s}$, the low-level upward motion, whose center is located a little downwind of the initial heating center, strengthens and the upstream and downstream tilt of the region of upward motion above the heating height appears. Above this bowl-shaped region of upward motion, a similarly shaped downward motion is produced in the process of the development of upward-propagating gravity waves. As time progresses, alternating regions of weak upward and downward motion are continuously produced (Figs. 1c,d). The tilting slope of the perturbation becomes small with time and hence the overall pattern becomes flat with time. The perturbation group that is produced by the initial pulse forcing and whose center propagates downwind continuously with a speed equal to the basic-state wind speed is called the moving mode (Baik et al. 1999b) or propagating mode (Hamilton et al. 1998). The moving mode forced by the pulse forcing in a uniform flow (the y -directional component of the basic-state wind is not considered) exhibits an axisymmetric field around a moving axis of $x = Ut$ and $y = 0$. This is apparent from the solutions to the surface and finite-depth pulse forcing given by (A7) and (A9), respectively. Both the solutions satisfy the relation of

$$w(x + Ut, y, z, t) = w(-x + Ut, -y, z, t). \quad (12)$$

As in the 2D transient problem in a uniform (Lin and Smith 1986) or shear (Baik et al. 1999b) flow with pulse forcing, the magnitude of the perturbation vertical velocity near the center of the moving mode increases rapidly at the initial stage, decreases a little, and then remains constant with time (Fig. 1). On the other hand, the magnitudes of the vertical displacement and the perturbation horizontal velocity increase linearly with time (not shown). These are apparent from the solution for the perturbation vertical velocity given by (A7) and the solutions for the vertical displacement and the perturbation horizontal velocity that can be obtained analytically. For large t ,

$$w_{3D,p}(Ut, 0, h, t) \rightarrow F, \quad (13a)$$

$$\eta_{3D,p}(Ut, 0, h, t) \rightarrow Ft, \quad (13b)$$

$$u_{3D,p}(x \approx Ut, 0, h, t) \rightarrow \left(2CN \int_0^{2\pi} \cos \theta \sin 3\varphi / X^3 d\theta \right) t, \quad (13c)$$

where

$$F = \frac{gq_0}{c_p T_0 a_x N}, \quad X = \sqrt{a_x^2 + [(Ut - x) \cos \theta]^2},$$

$$\varphi = \arctan \frac{(Ut - x) \cos \theta}{a_x}.$$

In two dimensions, when t is large, $w_{2D,p}(Ut, h, t) \rightarrow F/2$, $\eta_{2D,p}(Ut, h, t) \rightarrow (F/2)t$, and $u_{2D,p}(x \approx Ut, h, t) \rightarrow$

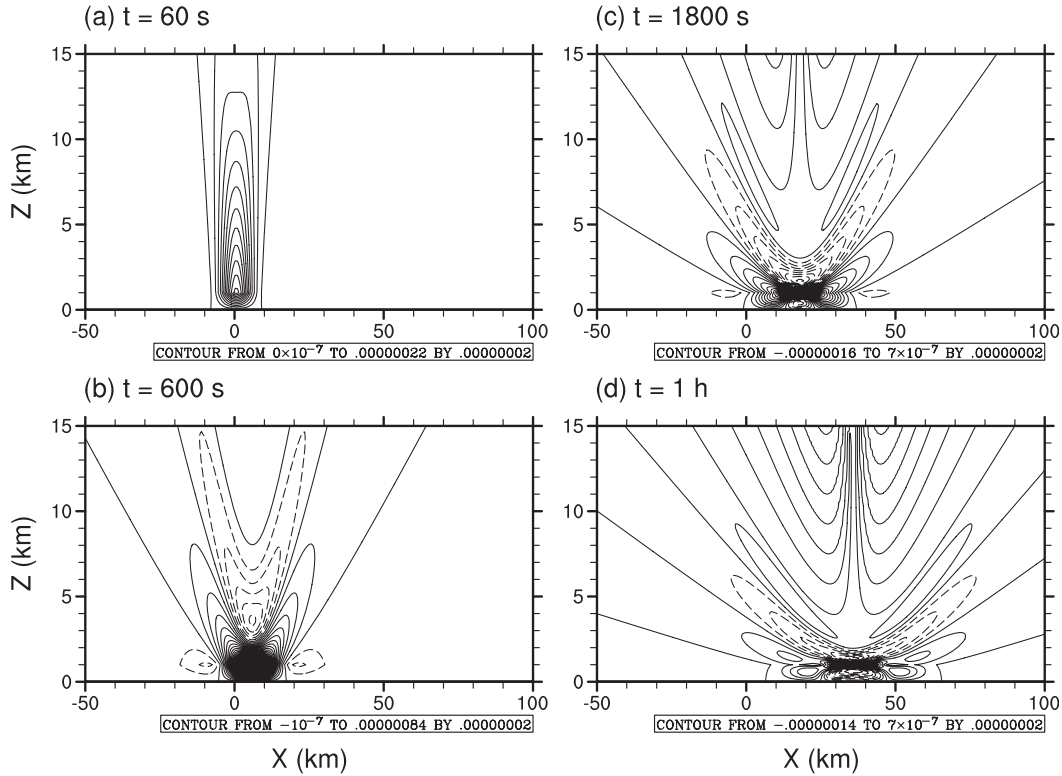


FIG. 1. The time evolution of the perturbation vertical velocity field along $y = 0$ when the surface pulse heating is applied at $z = 1$ km: $t =$ (a) 60 s, (b) 600 s, (c) 1800 s, and (d) 1 h. The specified parameter values are $U = 10 \text{ m s}^{-1}$, $V = 0 \text{ m s}^{-1}$, $N = 0.01 \text{ s}^{-1}$, $T_0 = 273 \text{ K}$, $q_0 = 2 \text{ J m kg}^{-1}$, and $a_x = a_y = 10 \text{ km}$. The heating center is located at $(x, y, z) = (0 \text{ km}, 0 \text{ km}, 1 \text{ km})$. The contour interval is $2 \times 10^{-8} \text{ m s}^{-1}$.

$(C'N\sin 2\varphi'/X'^2)t$ in a uniform flow (Lin and Smith 1986) and $w_{2D,p}(U_h t, h, t) \rightarrow FN/(2\alpha\mu)$, $\eta_{2D,p}(U_h t, h, t) \rightarrow [FN/(2\alpha\mu)]t$, and $u_{2D,p}(U_h t, h, t) \rightarrow [FN/(4\mu)]t$ in a shear flow with a domain unbounded in the vertical (Baik et al. 1999a), where U_h is the basic-state wind speed at the surface forcing height, α is the vertical wind shear, and $\mu = (N^2/\alpha^2 - 1/4)^{1/2}$ [note that $F = FN/(\alpha\mu)$ for $\alpha = 0$]. That is, both the value that the vertical velocity at the center of the moving mode converges to and the increasing rate of the vertical displacement at the center of the moving mode in two dimensions are half of those in three dimensions.

Using group velocity arguments, Bretherton (1988) showed that in three dimensions the vertical displacement at the center of the pulse heat source [$\eta_{3D,p}(0, 0, h, t)$] decays faster than $t^{-3/2}$ for large t . Through a rather difficult asymptotic analysis, which is not explicitly described, he indicated that $\eta_{3D,p}(0, 0, h, t)$ actually decreases as t^{-2} for large t . In this study, the solution for the vertical displacement to the surface pulse forcing, which can be obtained analytically from (11) using the relationship of $\hat{w} = (s + ikU + iIV)\hat{\eta}$ and the inverse transforms, shows that $\eta_{3D,p}(0, 0, h, t)$ is expressed by

$$\eta_{3D,p}(0, 0, h, t) = \int_0^{2\pi} \frac{2Ct}{X^3} \left\{ \begin{bmatrix} \frac{2Nth}{X} \cos\left(\frac{2Nth}{X} \sin \varphi - 4\varphi\right) \\ -\cos\left(\frac{2Nth}{X} \sin \varphi - 3\varphi\right) \end{bmatrix} e^{-2Nth \cos \varphi/X} + \cos 3\varphi \right\} d\theta, \quad (14)$$

where $X = [a_x^2 + (U \cos \theta)^2]^{1/2}$ and $\varphi = \arctan(U \cos \theta/a_x)$. Equation (14) reveals that $\eta_{3D,p}(0, 0, h, t)$ decreases as

fast as t^{-2} for large t (note that X is proportional to t for large t). This decay rate of the vertical displacement in

TABLE 1. Specified parameter values used in both the surface pulse heating case (section 3a) and finite-depth steady or transient heating case (section 3b).

Parameter	Value
x -directional basic-state horizontal wind speed (U)	10 m s^{-1}
y -directional basic-state horizontal wind speed (V)	0 m s^{-1}
Buoyancy frequency (N)	0.01 s^{-1}
Reference temperature (T_0)	273 K
Parameter that determines the x -directional horizontal size of the thermal forcing (a_x)	10 km
Parameter that determines the y -directional horizontal size of the thermal forcing (a_y)	10 km

three dimensions is different from that in two dimensions [$\eta_{2D,p}(0, h, t)$], showing the t^{-1} dependence. In two dimensions, the vertical displacement at the center of the steady heating, which is obtained by integrating $\eta_{2D,p}(0, h, t)$ with respect to time, increases logarithmically with time; hence, the steady state cannot be achieved without a widespread cooling term that makes the net heating at each level be zero (Smith and Lin 1982). However, in three dimensions, the steady state is approached without any conditions because the vertical displacement at the center of the steady heating decays as t^{-1} for large t . The faster decay rate of the vertical displacement in three dimensions results from the dispersion of gravity wave energy in the y direction (Bretherton 1988).

b. Finite-depth steady or transient heating case

In this subsection, the response of a stably stratified flow to the finite-depth steady or transient heating is examined. The response to the finite-depth steady or transient heating can be considered as the sum of an infinite number of responses of a stably stratified flow to surface pulse heating (Baik et al. 1999b).

Figure 2 shows the time evolution of the perturbation vertical velocity field along $y = 0$ when the finite-depth steady heating distributed uniformly from $z = 1$ to 9 km exits. At $t = 60$ s, a vertically extended upward motion having its maximum value at a height of $z = 7.1$ km is observed in a localized region near the heating center. A weak downward motion required to satisfy mass continuity exists over a wide region surrounding the upward motion. As time progresses, the region of upward motion expands over a wider region, especially in the downwind direction. Accordingly, the region of compensating downward motion becomes located farther away from the heating region. At $t = 600$ s, the upward motion extending over the steady heating layer

intensifies greatly. As upward-propagating gravity waves develop, the region of upward motion above the heating top tilts, and above that region a weak downward motion appears. At $t = 1800$ s, a main updraft region extending over the steady heating layer is slightly bent and has two local maxima at heights of $z = 3.0$ and 6.6 km, of which the lower one has the stronger intensity (this feature is revealed with a smaller contour interval). The downward motion observed above the main updraft region intensifies, and above that region alternating regions of upward and downward motion with a weak intensity appear. On the downwind side not far from the heating center and below the heating bottom height, the region of weak downward motion is produced. This region extends farther downwind as time progresses. The vertical velocity field at $t = 1$ h shows a clear distinction between a stationary mode [a group of perturbations with zero or near-zero horizontal phase speeds forced by each pulse forcing that is applied at different times (Hamilton et al. 1998; Baik et al. 1999b)] and a moving mode. The moving mode is observed in the downwind region centered at $x = 36$ km with a very small magnitude compared with the stationary mode. In the stationary mode, two distinctly separated local maxima in the main updraft region are observed. Perturbations above the heating top are tilted upstream, implying the upward propagation of wave energy. After $t = 1$ h, little change occurs in the perturbation pattern of the stationary mode (Figs. 2d–f). The center of the moving mode continues to move downwind with a speed equal to the basic-state wind speed, as in the pulse heating case.

The appearance of two local maxima in the main updraft region (Figs. 2c–f) is related to the vertical wavelength of gravity waves. The vertical wavelength of 3D, linear, hydrostatic internal gravity waves whose wave fronts are perpendicular to the basic-state wind direction in a steady state is $2\pi U/N$. With the specified parameter values in Fig. 2, the calculated vertical wavelength is 6.28 km. The flow response field near the heating center shows that the sign of perturbations above the heating top is changed every 3.14 km in the vertical (see Fig. 2e). Near the height where the surface steady heating is applied, an upward motion of relatively strong intensity is produced in the concentrated heating region. Hence, in the case of finite-depth steady heating, in which the response can be considered as the sum of an infinite number of responses to surface steady heating that is applied at different heights, a main updraft region extending over the steady heating layer is produced. In the region where upward- and downward-propagating gravity waves are combined to yield a negative magnitude, the upward motion weakens there. On the other hand, in the region where upward- and

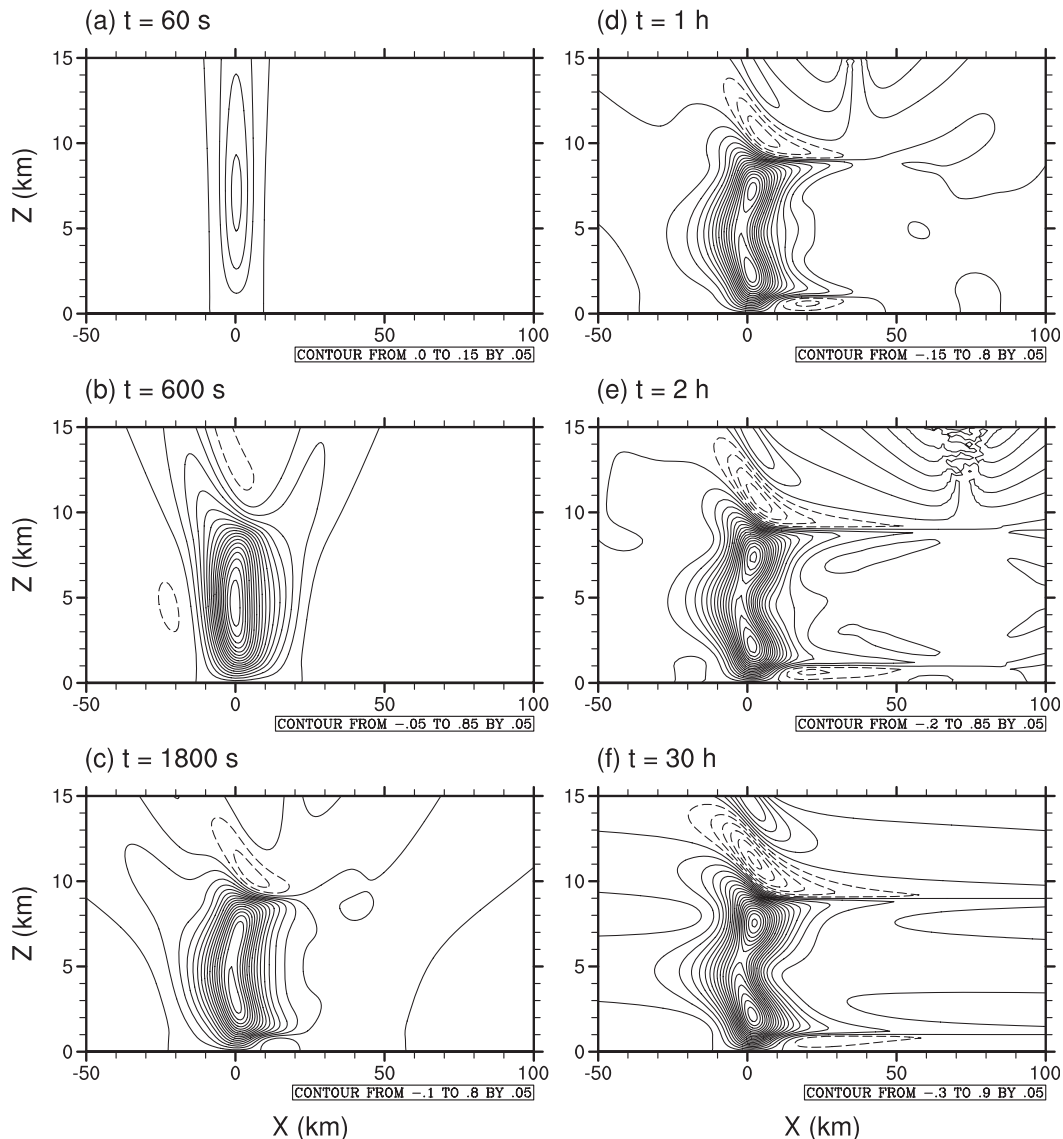


FIG. 2. The time evolution of the perturbation vertical velocity field along $y = 0$ when the finite-depth steady heating distributed uniformly from $z = 1$ to 9 km exists: $t =$ (a) 60 s, (b) 600 s, (c) 1800 s, (d) 1 h, (e) 2 h, and (f) 30 h. The contour interval is 0.05 m s^{-1} . In the finite-depth steady or transient heating case, q_0 is $2 \text{ J kg}^{-1} \text{ s}^{-1}$.

downward-propagating gravity waves are combined to yield a positive magnitude, the upward motion strengthens there. This results in two local maxima. For a higher heating top height, a weaker basic-state wind, or a more stable atmosphere, we confirmed that two or more maxima are observed in the main updraft region.

At all levels, the initial response field shows a circular upward motion that centers the heating center and is enclosed by a weak compensating downward motion (Figs. 3a and 4a). As time progresses, however, the flow patterns at each level, especially in and above the steady heating layer, evolve differently. Figure 3 shows the time evolution of the perturbation vertical velocity field

at the middle of the heating layer (i.e., $z = 5$ km). The perturbation field is symmetric about $y = 0$ because only the x -directional component of the basic-state wind is considered. At $t = 600$ s, the circular upward motion, which has its maximum at the center of the heating, intensifies and occupies a wider area, especially in the downwind direction. With time, the region of circular upward motion having the same center as the moving mode widens. Within this region, a relatively strong upward motion is elongated in the direction perpendicular to the basic-state wind near the concentrated heating region. At $t = 1$ h, a ring-shaped region of weak downward motion encircles the center of the moving mode on

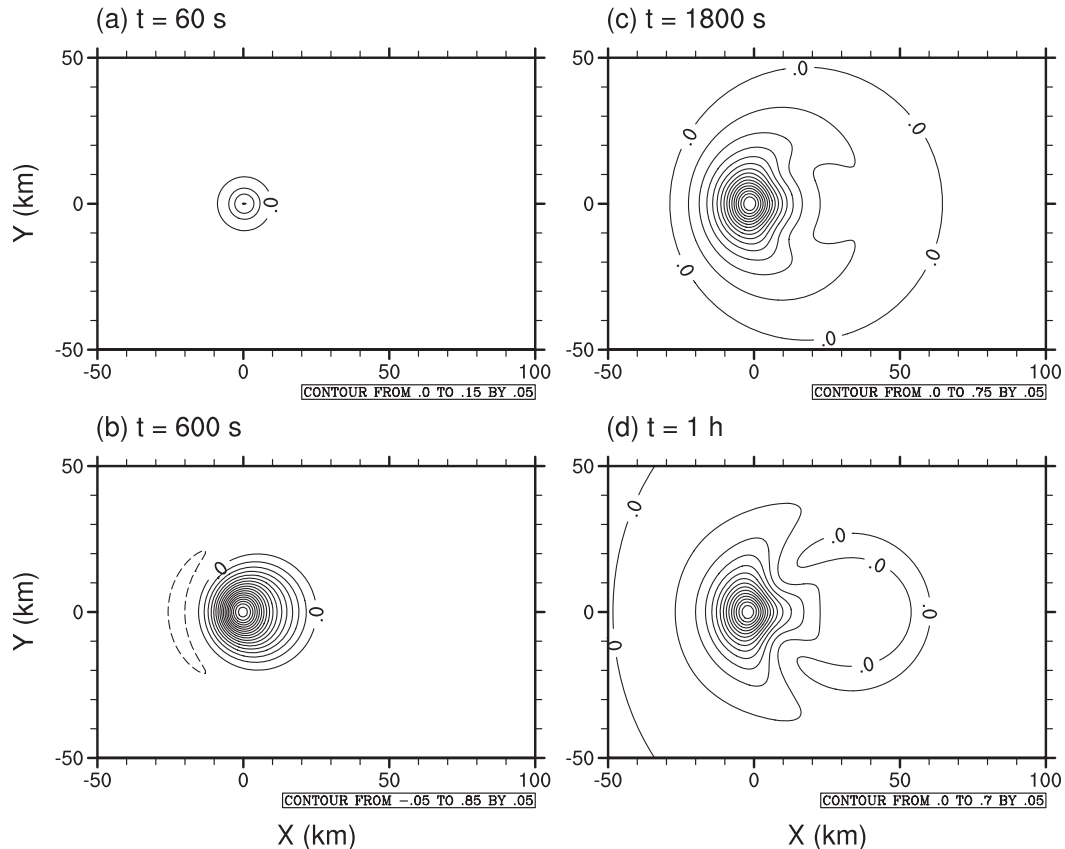


FIG. 3. The time evolution of the perturbation vertical velocity field at the middle of the heating layer (i.e., $z = 5$ km) when the finite-depth steady heating distributed uniformly from $z = 1$ to 9 km exits: $t =$ (a) 60 s, (b) 600 s, (c) 1800 s, and (d) 1 h. The contour interval is 0.05 m s^{-1} .

the downwind side. As time progresses, this region of ring-shaped downward motion extends over a wider area in the downwind direction.

Figure 4 shows the time evolution of the perturbation vertical velocity field at a height of $z = 10$ km. At $t = 600$ s, the flow response field above the steady heating layer shows—unlike in the steady heating layer (Fig. 3b)—that there exist maximum and minimum upward motions upwind and downwind of the heating center, respectively, within the region of circular upward motion. The upward motion is much weaker but spreads over a wider area compared with that in the steady heating layer. In the process of the development of upward-propagating gravity waves above the heating top, the magnitude of local minimum upward motion on the downwind side decreases, and finally a circular downward motion appears in that region (Fig. 4c). The region of the maximum upward motion on the upwind side is split into two regions of upward motion. One region includes upward motion that becomes very weak as it slowly propagates in the upwind direction. The other region develops into a V-shaped upward motion of relatively strong inten-

sity, which stays near the concentrated heating region (Figs. 4c,d). At $t = 1$ h, a V-shaped downward motion also appears within the region of circular downward motion that extends over a wide area on the downwind side as time progresses. The eventual response in the stationary mode at $z = 10$ km is the V-shaped upward and downward motions that are dominant upwind and downwind of the heating center, respectively. The perturbation vertical velocity at $z = 13.14$ km (10 km plus half of the vertical wavelength of gravity waves) exhibits a reverse of that at $z = 10$ km. That is, the V-shaped upward (downward) motion, which is weaker and wider in the y -direction than below, is dominant downwind (upwind) of the heating center (not shown).

Lin (1986) indicated that V-shaped clouds observed at the top of deep convective storms can be explained by V-shaped upward and downward motion associated with upward-propagating gravity waves. The V-shaped signature is also observed in the flow response field below the height of the heating bottom by the action of downward-propagating and reflected upward-propagating gravity waves. The V-shaped features above and below

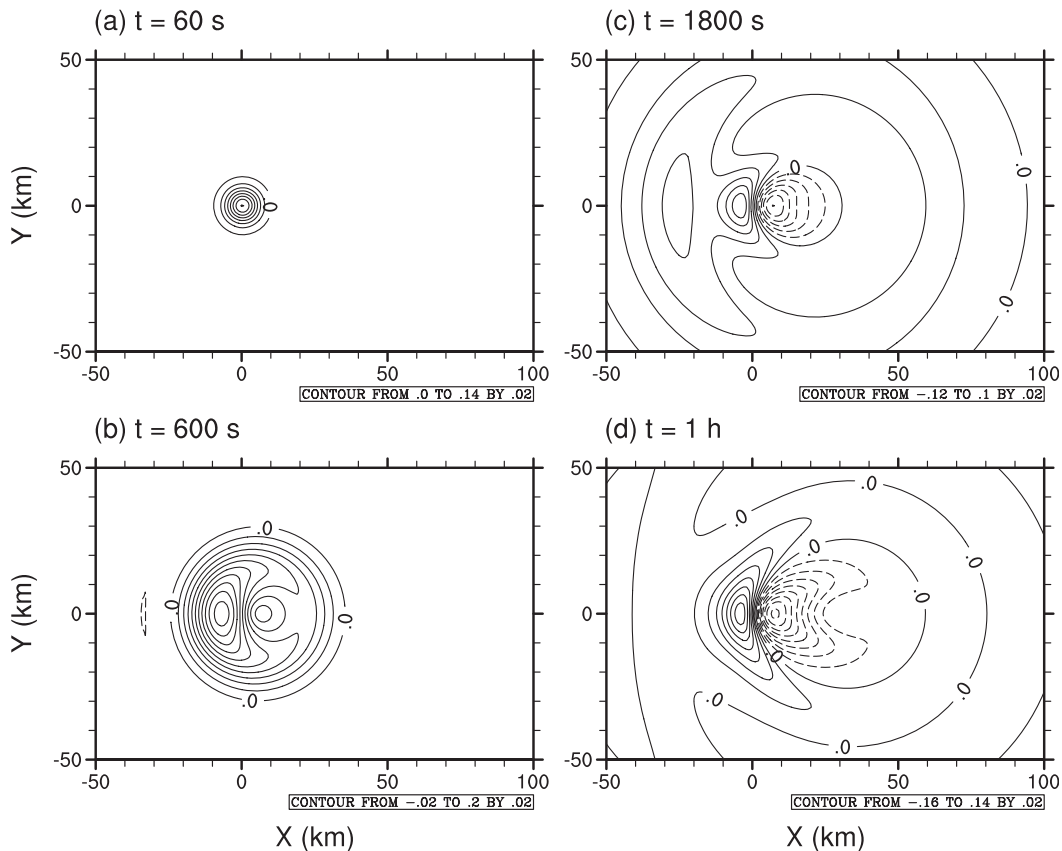


FIG. 4. As in Fig. 3, but for $z = 10$ km. The contour interval is 0.02 m s^{-1} .

the steady heating layer can be explained using group velocity arguments, as in the mountain wave problem (Smith 1980). Smith (1980) showed that at each level aloft there is considerable wave energy along the parabola $y^2 = Nzax/U$ (a is a mountain horizontal scale) for the hydrostatic steady flow over a bell-shaped isolated mountain. This is also true for the flow forced by steady thermal forcing. Note that the thermally forced vertical velocity field in Fig. 4d is very similar to the orographically forced vertical velocity field shown by Smith (1980) in his Fig. 1. That is, the characteristics of the flow far from the mountain, including not only the V-shaped signature but also the radial outward tilting phase lines and the decrease in magnitude away from the source region (Smith 1980), also appear in the flow response field above the steady heating layer.

The Coriolis acceleration terms are not included in the governing equations of this study. Convectively forced mesoscale flows can be influenced by the Coriolis force, especially when convection persists for a long time. Although obtaining solutions in physical space in the case with the Coriolis acceleration terms seems very difficult, it deserves a future study.

The gravity wave momentum flux is calculated to examine its vertical variation. Figure 5 shows the vertical profile of the vertical flux of the integrated zonal momentum \overline{uw} at $t = 2$ h for the case corresponding to Fig. 2. Here, the overbar denotes the integration over the x - y plane. Previous steady-state studies in a bounded domain below (Smith and Lin 1982; Chun and Baik 1998) indicate that below the heating bottom, there exists a complete cancellation of momentum fluxes of downward-propagating gravity waves that come directly from the heating layer and reflected upward-propagating gravity waves; hence, the integrated momentum flux becomes zero. However, in this transient problem with a bounded domain below, the integrated momentum flux below the heating bottom is positive, with decreasing magnitude from the heating bottom to $z = 0$. This is similar to the result of the transient problem in a vertically unbounded domain (Lin and Smith 1986), but with smaller magnitude due to reflected upward-propagating gravity waves and zero momentum flux at the surface in the presence of the flat bottom boundary in the present study. The vertical profile of the momentum flux in the heating layer varies with time. At a very early stage, the

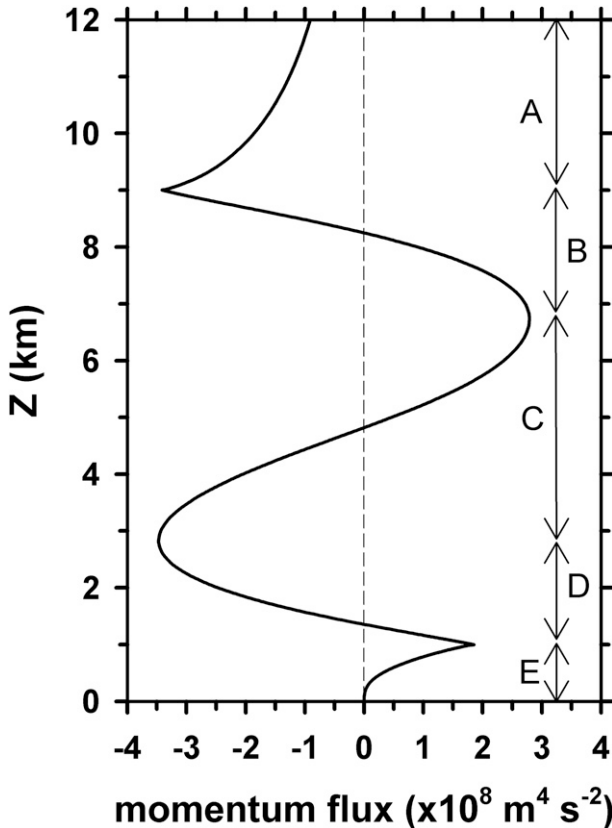


FIG. 5. The vertical profile of the vertical flux of the integrated zonal momentum ($\text{m}^4 \text{s}^{-2}$) at $t = 2$ h when the finite-depth steady heating distributed uniformly from $z = 1$ to 9 km exits. A, C, and E (B and D) are the layers in which the vertical divergence (convergence) of the momentum flux occurs.

momentum flux in the heating layer monotonically decreases with height from a relatively small positive value at the heating bottom to a negative value at the heating top. Hence, the vertical convergence of the momentum flux occurs in the heating layer (not shown). As time progresses, the momentum flux in the heating layer with height decreases at low levels, increases at middle levels, and then decreases again at upper levels (Fig. 5). Hence, a layer of the vertical divergence of the momentum flux near the middle of the heating layer is produced (layer C in Fig. 5). Also, note that there exists a vertical divergence of the momentum flux above and below the heating layer (layers A and E in Fig. 5). Above the heating top, the momentum flux is negative, implying that the wave energy is transported upward. The vertical flux of the integrated meridional momentum $\overline{v'w'}$ is zero because the y -directional perturbation velocity field is symmetric about $y = 0$ (but with opposite sign) and the perturbation vertical velocity field is symmetric about $y = 0$.

Next, we will compare 2D and 3D flows forced by convective heating in an effort to better understand the role of three-dimensionality. Figure 6 shows the time evolution of the perturbation vertical velocity field in two dimensions when the finite-depth steady heating exits. The solution for the perturbation vertical velocity in two dimensions is given in appendix B. Early response fields in two dimensions show a relatively strong upward motion near the heating region and a weak compensating downward motion on both sides of the upward motion (Figs. 6a,b). These features are generally similar to those in three dimensions. However, the upward motion extending over the steady heating layer is of weaker intensity than that in three dimensions because the low-level convergence in the y -direction does not exist in two dimensions. A stronger compensating downward motion in two dimensions is explained by the fact that there is no compensating downward motion in the y -direction in two dimensions. At $t = 1800$ s, the intensity of the main updraft region in two dimensions becomes similar to that in three dimensions. At $t = 1$ h, one maximum in the upward motion is observed in two dimensions, whereas two local maxima in the upward motion appear in three dimensions (Figs. 2d and 6d). As time progresses further, the main updraft region in two dimensions that becomes stronger than that in three dimensions also shows two local maxima at heights of $z = 4.5$ and 7.1 km (this feature is revealed with a smaller contour interval in Fig. 6e). As stated previously, the perturbation vertical velocity field in the stationary mode in three dimensions shows a main updraft region that extends over the steady heating layer and whose pattern remains similar after $t = 1$ h. In two dimensions, however, the main updraft region is split into two regions of upward motion as the downward motions located at the low-level upwind region, downwind of the middle of the heating layer, and upwind of the upper part of the heating layer, develop with time (Fig. 6f). It is apparent from Fig. 6f that the appearance of two regions of maximum upward motion in the steady heating layer is related to the vertical wavelength of gravity waves. Because there is no y -directional dispersion of gravity wave energy in two dimensions, after some time the upward-propagating stationary gravity wave field above the heating top in two dimensions exhibits a much stronger vertical velocity than in three dimensions (Figs. 2f and 6f).

The perturbation vertical velocity field at a sufficiently large time calculated using our 2D transient solution exhibits some different features from that calculated using the 2D steady-state solution of Chun and Baik (1998) with the same parameter values. The

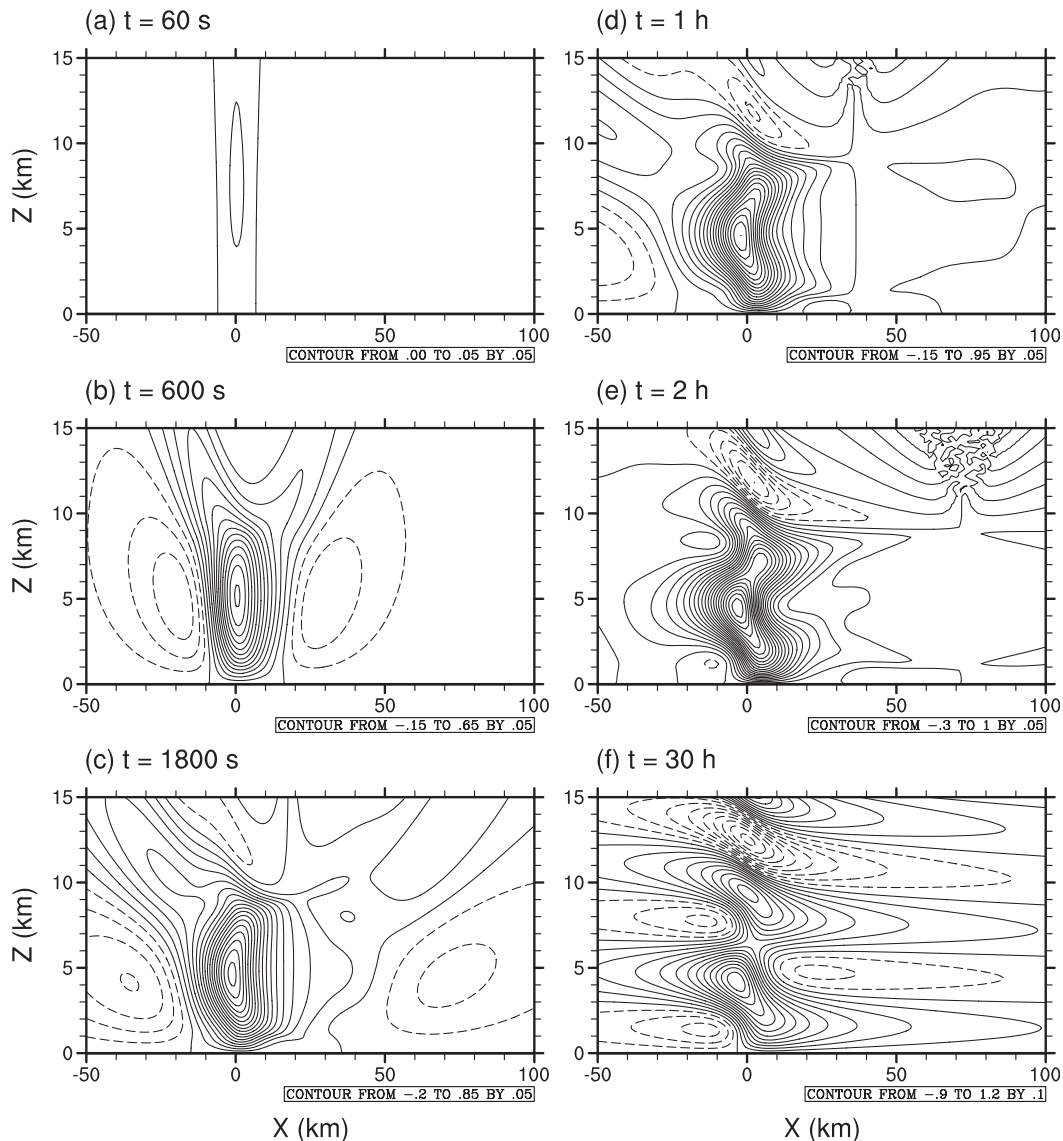


FIG. 6. The time evolution of the perturbation vertical velocity field in two dimensions when the finite-depth steady heating distributed uniformly from $z = 1$ to 9 km exits: $t =$ (a) 60 s, (b) 600 s, (c) 1800 s, (d) 1 h, (e) 2 h, and (f) 30 h. The contour intervals are 0.05 m s^{-1} in (a)–(e) and 0.1 m s^{-1} in (f).

stationary gravity wave field of relatively strong intensity calculated using the steady-state solution is more confined near the steady heating region than that at a sufficiently large time calculated using our transient solution. The region of maximum upward motion in the steady heating layer and the upward-propagating stationary gravity wave field above the heating top have weaker intensities in the steady-state solution than in the transient solution, whereas the region of compensating downward motion has a stronger intensity. These differences are related to a widespread cooling term that is necessary to avoid a net heating problem in a 2D, steady-state, nonrotating, inviscid airflow system (Smith

and Lin 1982), which is included in the steady-state problem of Chun and Baik (1998) but not included in our transient problem. It was found that the stationary gravity wave field calculated using the steady-state solution is about the same as that at a sufficiently large time calculated using the transient solution to the problem that includes a widespread cooling term.

Figure 7 shows the perturbation vertical velocity at the heating bottom height ($z = 1$ km) at $t = 2$ h as a function of the basic-state wind speed in two and three dimensions (along $y = 0$). In two dimensions, downward motion appears near the heating center for large basic-state wind speed. However, in three dimensions, upward

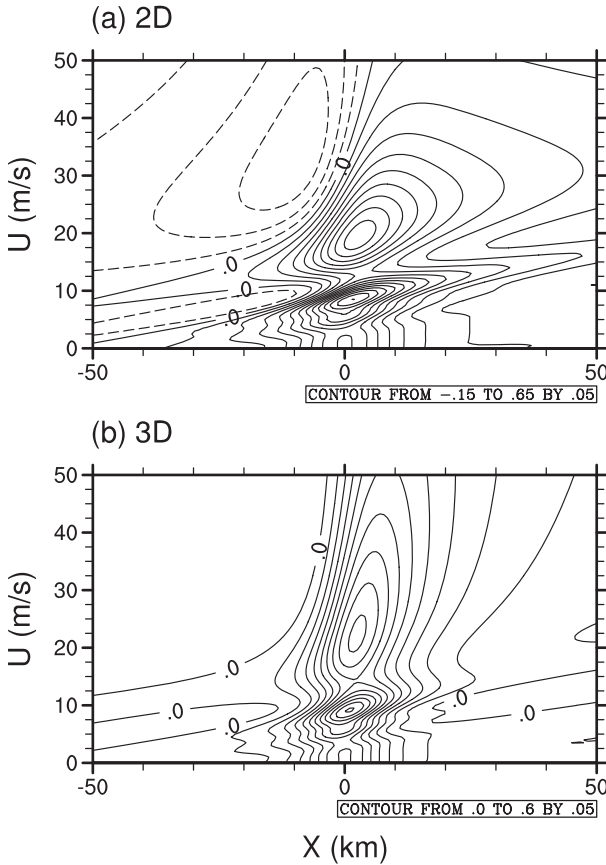


FIG. 7. The perturbation vertical velocity at the heating bottom height ($z = 1$ km) at $t = 2$ h as a function of the basic-state wind speed in (a) two and (b) three dimensions (along $y = 0$) when the finite-depth steady heating distributed uniformly from $z = 1$ to 9 km exits. The contour interval is 0.05 m s^{-1} .

motion is always observed near the heating center regardless of the basic-state wind speed. This is consistent with the result of Lin (1986). The upward motion that exists below the steady heating layer can act to sustain deep moist convection by transporting low-level moisture upward (Mapes 1993). The non-monotonous variation in the magnitude of the upward motion near the heating center with varying basic-state wind speed is a result of changes in the level, where direct downward-propagating and reflected upward-propagating waves are combined to result in large magnitudes, along with changes in the vertical wavelength of gravity waves.

To examine the dependence of convectively forced flows on the vertical structure of convective heating, we obtain solutions for various shapes of vertical heating profile. The vertical heating profile considered is

$$f(z) = A \sin(\pi\eta) \exp(b\eta) \quad \text{for } h_1 \leq z \leq h_2, \quad (15)$$

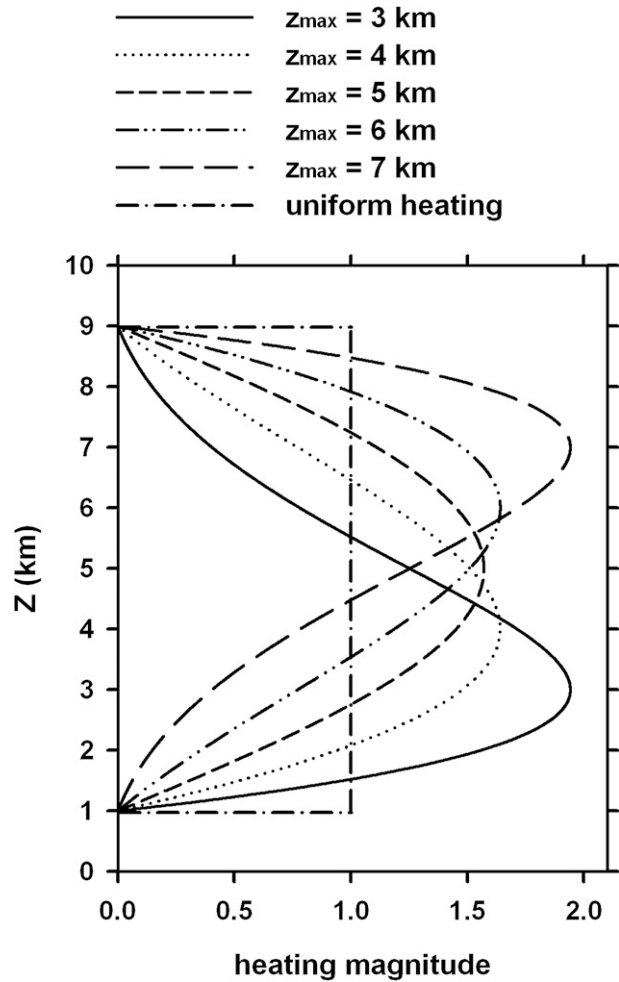


FIG. 8. The vertical heating profiles given by (15) with various z_{\max} . The case of uniformly distributed heating is also plotted for comparison.

where

$$\eta(z) = \frac{z - h_1}{h_2 - h_1}, \quad b = -\frac{\pi}{\tan[\pi(z_{\max} - h_1)/(h_2 - h_1)]}.$$

Here, z_{\max} is the height of the maximum heating and A is determined to have the same total amount of heating as the thermal forcing distributed uniformly from $z = h_1$ to h_2 , yielding $A = (b^2 + \pi^2)/[\pi(e^b + 1)]$. The vertical heating profile (15) is similar to that used in a study of the linear response of the large-scale tropical atmosphere to convective forcing by DeMaria (1985). The vertical profiles of heating with various z_{\max} are plotted in Fig. 8.

Figures 9a–e show the perturbation vertical velocity fields along $y = 0$ at $t = 2$ h in the cases of vertically nonuniform steady heating with $z_{\max} = 3, 4, 5, 6$, and 7 km. Unlike the uniform heating case (Fig. 9f) in which

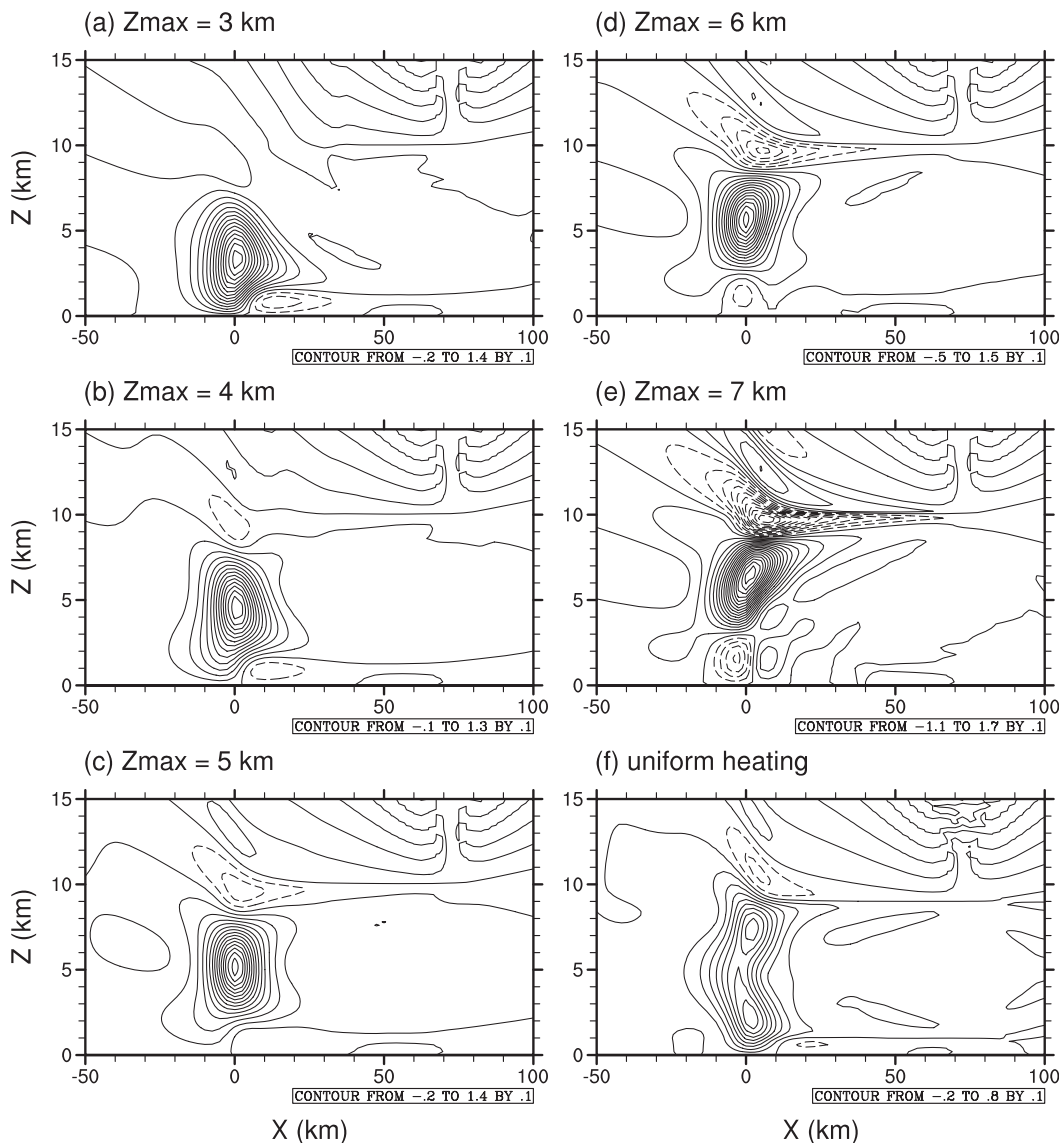


FIG. 9. The perturbation vertical velocity fields along $y = 0$ at $t = 2$ h when the vertically nonuniform steady heating given by (15) with $z_{\max} =$ (a) 3, (b) 4, (c) 5, (d) 6, and (e) 7 km exits. The case of uniformly distributed heating is also plotted in (f) for comparison. The contour interval is 0.1 m s^{-1} .

two local maxima in the main updraft region are observed, there is only one maximum in all nonuniform heating cases. As should be expected, the height of the maximum upward motion increases as the height of the maximum heating increases, but its location does not exactly coincide with the height of the maximum heating. When the maximum heating is located below the middle of the heating layer ($z = 5$ km), the maximum updraft is observed a little above the maximum heating height (Figs. 9a,b). On the other hand, when the maximum heating is present above the middle of the heating layer, the maximum updraft appears a little below the maximum heating height (Figs. 9d,e). As the height of the

maximum heating increases, the field of the stationary gravity wave above the heating top, which shows alternating regions of upward and downward motion with an upstream phase tilt, becomes stronger in its intensity. In the cases with a lower altitude of the maximum heating (Figs. 9a–c), the region of weak low-level downward motion is observed on the downwind side, as in the uniform heating case. However, as the height of the maximum heating increases further (Fig. 9d), it is extended up to the steady heating region. When the height of the maximum heating is 7 km (Fig. 9e), more intensified low-level downward motion is located upwind of the heating center and a weak upward motion appears on its downwind side.

So far, we have considered that the heating is constant with time. However, in the real atmosphere, the amplitude of convective heating changes during the life cycle of convection. Therefore, it is necessary to consider transient convective heating reflecting the life cycle of deep convection and investigate its influence on convectively forced flows. The transient heating function used in this study is

$$g(t) = \alpha t^2 \exp(-\beta t). \quad (16)$$

Here, we let the maximum heating occur at $t = 1$ h and let the total heating amount over 3 h be equal to that in the steady heating case. This yields $\beta = 2 \text{ h}^{-1}$ and $\alpha = \int_0^{3\text{h}} 1 dt / \int_0^{3\text{h}} t^2 e^{-\beta t} dt$. A similar transient heating function is used in a study of the linear response of the large-scale tropical atmosphere to transient convection by Silva Dias et al. (1983). The function $g(t)$ is plotted in Fig. 10. It is assumed that the amplitude of convective heating increases with time as a convective system develops, peaks at a mature stage, and then gradually decreases at a dissipation stage.

Figure 11 shows the time evolution of the perturbation vertical velocity field along $y = 0$ when the finite-depth transient heating exits. The magnitude of the upward motion extending over the heating layer changes with the amplitude of transient heating. This is contrasted with the steady heating case in which, although the heating is constant with time, the upward motion intensifies rapidly at a very early stage, weakens a little, and then strengthens again very slowly, reaching a quasi-steady state. At early times when the heating amplitude is weaker than that in the steady heating case, the upward motion near the heating region has a much weaker intensity and develops more slowly than in the steady heating case. However, because the upward motion keeps strengthening while the heating amplitude increases, the maximum upward motion that occurs near the time of the maximum amplitude of transient heating (i.e., $t = 1$ h) becomes much stronger than that in the steady heating case (Figs. 2d and 11b). As the amplitude of transient heating decreases, the magnitude of the upward motion also continues to decrease. The flow pattern until $t = 2$ h shows no significant difference compared with that in the steady heating case. In particular, the flow response field at $t = 2$ h is very similar to the stationary gravity wave field in the steady heating case (Figs. 9f and 11c). However, as the heating amplitude decreases further, the downward motion that develops between regions of two local maxima in the upward motion causes the main updraft region to be separated into two regions of upward motion (Figs. 11d–f). Hence, alternating regions of upward and downward motion with an upstream phase tilt appear

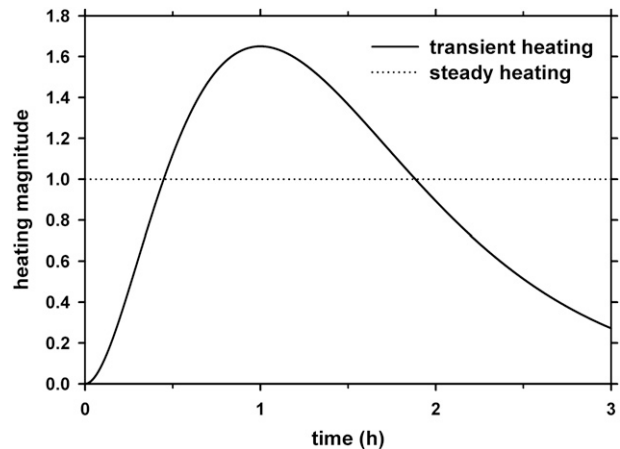


FIG. 10. The transient heating function given by (16). The case of steady heating is also plotted for comparison.

like those above the heating top, but with a maximum located not near the heating center but on the downwind side.

4. Summary and conclusions

In this study, convectively forced mesoscale flows in three dimensions were theoretically investigated by examining the transient response of a stably stratified uniform flow to deep convective heating. The airflow system considered is a 3D, time-dependent, hydrostatic, nonrotating, inviscid, Boussinesq system with a uniform basic-state wind and a constant buoyancy frequency. The analytic solution to the finite-depth steady or transient heating that represents latent heating due to cumulus convection was obtained by integrating the solution to the surface pulse heating, and both solutions were analyzed to better understand the characteristics of stationary and moving modes forced by convective heating.

In the surface pulse heating case, the flow response field is axisymmetric around the moving axis that continues to move downwind with a speed equal to the basic-state wind speed. As in the 2D transient problem in a uniform or shear flow, the perturbation vertical velocity near the center of the moving mode remains constant after some time, whereas the vertical displacement and the perturbation horizontal velocity increase linearly with time. However, both the value that the perturbation vertical velocity at the center of the moving mode converges to and the increasing rate of the vertical displacement at the center of the moving mode in three dimensions are twice those in two dimensions. It was explicitly shown that in three dimensions the vertical displacement at the center of the steady heating obtained by integrating the vertical displacement at the center of the pulse heating with respect to time decays

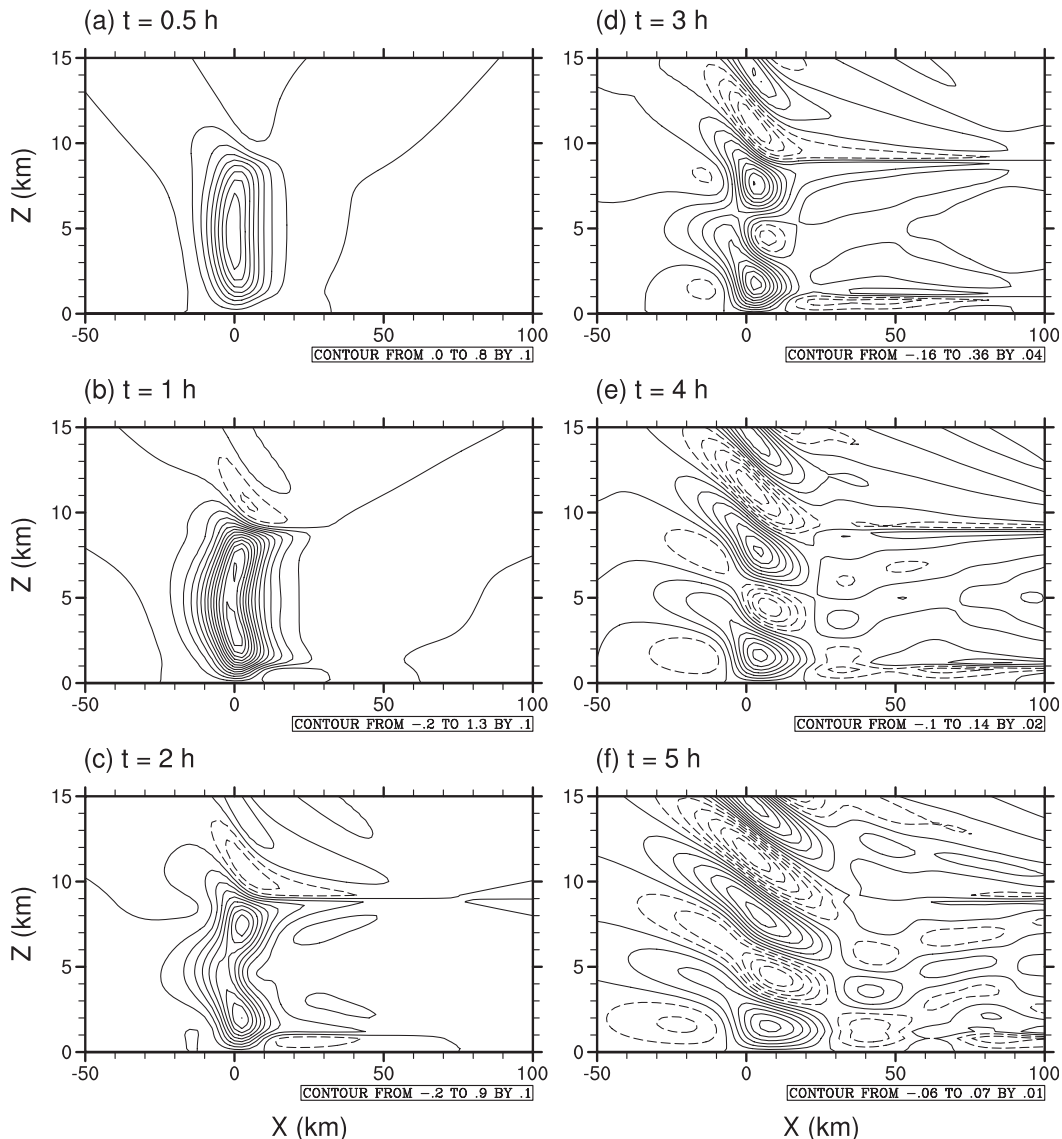


FIG. 11. The time evolution of the perturbation vertical velocity field along $y = 0$ when the finite-depth transient heating given by (16) exits: $t =$ (a) 0.5, (b) 1, (c) 2, (d) 3, (e) 4, and (f) 5 h. The contour intervals are 0.1 m s^{-1} in (a)–(c), 0.04 m s^{-1} in (d), 0.02 m s^{-1} in (e), and 0.01 m s^{-1} in (f).

as t^{-1} for large t . Therefore, unlike in two dimensions, the steady state is achieved in three dimensions without a widespread cooling term.

The response to the finite-depth steady heating shows a main updraft region that extends over the heating layer and V-shaped upward and downward motions above and below the heating layer in the stationary mode. The vertical flux of the integrated zonal momentum is negative above the heating top and positive below the heating bottom, with decreasing magnitude away from the heating layer; hence, the vertical divergence of the momentum flux occurs there. The momentum flux inside the steady heating layer decreases

with height at low levels, increases at middle levels, and then decreases again at upper levels, resulting in a layer of the vertical divergence of the momentum flux near the middle of the heating layer. Including the third dimension leads to a stronger upward motion at early times, a weaker compensating downward motion, and a weaker upward-propagating stationary gravity wave field in a quasi-steady state than in two dimensions. From the solutions for various shapes of vertical heating profile, it was shown that as the height of the maximum heating increases, the field of the stationary gravity wave above the heating top becomes stronger in its intensity. In the finite-depth transient heating case reflecting the life cycle

of deep convection, the vertical velocity at a dissipation stage does not exhibit a main updraft region extending over the heating layer anymore. Instead, alternating regions of upward and downward motion with an upstream phase tilt appear like those above the heating top.

In this study, we solved a 3D transient problem in a uniform flow and could understand some transient dynamics of convectively forced mesoscale flows. The real atmosphere, however, usually has a vertical shear of the basic-state horizontal wind with or without a critical level. The vertical shear can affect convectively forced flows. In Part II of this study, we will extend this uniform flow case to the case of a shear flow with a critical level and examine critical-level effects on convectively forced mesoscale flows in a 3D transient framework.

Acknowledgments. The authors are grateful to two anonymous reviewers for providing valuable comments. This work was funded by the Korea Meteorological Administration Research and Development Program under Grant CATER 2006-2202 and the BK21 project.

APPENDIX A

Analytic Solutions for the Perturbation Vertical Velocity in Three Dimensions

We perform the inverse Laplace transform in s ($\rightarrow t$) and the inverse double Fourier transform in k ($\rightarrow x$) and l ($\rightarrow y$) of (11) to get the solution in physical space. First, taking the inverse Laplace transform of (11a) gives

$$w_1(x, y, z, t) = \text{Re} \left\langle -C \int_{-\infty}^{\infty} \int_{-\infty}^{\infty} K e^{-\sqrt{k^2 a_x^2 + l^2 a_y^2}} \times \left\{ \sum_{n=0}^{\infty} \frac{[-NKt(z+h)]^n}{n!n!} - \sum_{n=0}^{\infty} \frac{[NKt(z-h)]^n}{n!n!} \right\} \times e^{-ikUt-ilVt} e^{ikx} e^{ily} dk dl \right\rangle. \quad (\text{A1})$$

To simplify calculation, (A1) is converted into an integral in polar coordinates. Then, (A1) becomes

$$w_1(x, y, z, t) = \text{Re} \left\langle -C \int_0^{2\pi} \left\{ \sum_{n=0}^{\infty} \frac{[-Nt(z+h)]^n}{n!n!} - \sum_{n=0}^{\infty} \frac{[Nt(z-h)]^n}{n!n!} \right\} \times \left(\int_0^{\infty} e^{-KT} K^{n+2} dK \right) d\theta \right\rangle, \quad (\text{A2})$$

where

$$T = a_x \sqrt{\cos^2 \theta + \gamma^2 \sin^2 \theta} + i[(Ut - x) \cos \theta + (Vt - y) \sin \theta], \\ \theta = \arctan(l/k), \quad \gamma = a_y/a_x.$$

After integration with respect to K , (A2) becomes

$$w_1(x, y, z, t) = \text{Re} \left\langle -C \int_0^{2\pi} \left\{ \sum_{n=0}^{\infty} \frac{[-Nt(z+h)]^n}{n!n!} - \sum_{n=0}^{\infty} \frac{[Nt(z-h)]^n}{n!n!} \right\} \frac{(n+2)!}{T^{n+3}} d\theta \right\rangle. \quad (\text{A3})$$

One can rewrite (A3) in a simpler form and finally get the solution for the perturbation vertical velocity to the surface pulse forcing for $0 \leq z \leq h$:

$$w_1(x, y, z, t) = \text{Re} \left\langle \begin{aligned} & C \int_0^{2\pi} e^{-Nt(z+h)/T} \left\{ -\frac{[Nt(z+h)]^2}{T^5} + \frac{4Nt(z+h)}{T^4} - \frac{2}{T^3} \right\} d\theta \\ & - C \int_0^{2\pi} e^{Nt(z-h)/T} \left\{ -\frac{[Nt(z-h)]^2}{T^5} - \frac{4Nt(z-h)}{T^4} - \frac{2}{T^3} \right\} d\theta \end{aligned} \right\rangle. \quad (\text{A4})$$

In a similar way, it can be shown that the solution for $z > h$ is

$$w_2(x, y, z, t) = \text{Re} \left\langle \begin{aligned} & C \int_0^{2\pi} e^{-Nt(z+h)/T} \left\{ -\frac{[Nt(z+h)]^2}{T^5} + \frac{4Nt(z+h)}{T^4} - \frac{2}{T^3} \right\} d\theta \\ & - C \int_0^{2\pi} e^{-Nt(z-h)/T} \left\{ -\frac{[Nt(z-h)]^2}{T^5} + \frac{4Nt(z-h)}{T^4} - \frac{2}{T^3} \right\} d\theta \end{aligned} \right\rangle. \quad (\text{A5})$$

Equations (A4) and (A5) can be written as a single equation that is valid for both $0 \leq z \leq h$ and $z > h$:

$$w(x, y, z, t) = \text{Re} \left\langle \begin{aligned} & C \int_0^{2\pi} e^{-Nt(z+h)/T} \left\{ -\frac{[Nt(z+h)]^2}{T^5} + \frac{4Nt(z+h)}{T^4} - \frac{2}{T^3} \right\} d\theta \\ & - C \int_0^{2\pi} e^{-Nt|z-h|/T} \left\{ -\frac{[Nt(z-h)]^2}{T^5} + \frac{4Nt|z-h|}{T^4} - \frac{2}{T^3} \right\} d\theta \end{aligned} \right\rangle. \quad (\text{A6})$$

Evaluating the real part of (A6) gives

$$\begin{aligned} w(x, y, z, t) &= C \int_0^{2\pi} e^{-B_+ \cos \varphi / X} \left[-\frac{B_+^2}{X^5} \cos \left(\frac{B_+}{X} \sin \varphi - 5\varphi \right) + \frac{4B_+}{X^4} \cos \left(\frac{B_+}{X} \sin \varphi - 4\varphi \right) - \frac{2}{X^3} \cos \left(\frac{B_+}{X} \sin \varphi - 3\varphi \right) \right] d\theta \\ &\quad - C \int_0^{2\pi} e^{-B_- \cos \varphi / X} \left[-\frac{B_-^2}{X^5} \cos \left(\frac{B_-}{X} \sin \varphi - 5\varphi \right) + \frac{4B_-}{X^4} \cos \left(\frac{B_-}{X} \sin \varphi - 4\varphi \right) - \frac{2}{X^3} \cos \left(\frac{B_-}{X} \sin \varphi - 3\varphi \right) \right] d\theta. \end{aligned} \quad (\text{A7})$$

Here,

$$\begin{aligned} B_+ &= Nt(z+h), \quad B_- = Nt|z-h|, \\ X &= \sqrt{a_x^2 (\cos^2 \theta + \gamma^2 \sin^2 \theta)^2 + [(Ut-x) \cos \theta + (Vt-y) \sin \theta]^2}, \quad \text{and} \\ \varphi &= \arctan \frac{(Ut-x) \cos \theta + (Vt-y) \sin \theta}{a_x \sqrt{\cos^2 \theta + \gamma^2 \sin^2 \theta}}. \end{aligned}$$

We obtain the solution for the perturbation vertical velocity to the finite-depth pulse forcing, which is distributed uniformly from $z = h_1$ to h_2 , by integrating (A6) with respect to the forcing level h :

$$\begin{aligned} w(x, y, z, t) &= \text{Re} \left\{ C \int_0^{2\pi} e^{-Nt(z+h_1)/T} (z+h_1) \left[\frac{2}{T^3} - \frac{Nt(z+h_1)}{T^4} \right] - e^{-Nt(z+h_2)/T} (z+h_2) \left[\frac{2}{T^3} - \frac{Nt(z+h_2)}{T^4} \right] d\theta \right. \\ &\quad \left. + C \int_0^{2\pi} e^{-Nt|z-h_1|/T} (z-h_1) \left[\frac{2}{T^3} - \frac{Nt|z-h_1|}{T^4} \right] - e^{-Nt|z-h_2|/T} (z-h_2) \left[\frac{2}{T^3} - \frac{Nt|z-h_2|}{T^4} \right] d\theta \right\}. \end{aligned} \quad (\text{A8})$$

Evaluating the real part of (A8) yields

$$\begin{aligned} w(x, y, z, t) &= C \int_0^{2\pi} e^{-B_{1+} \cos \varphi / X} (z+h_1) \left[\frac{2}{X^3} \cos \left(\frac{B_{1+}}{X} \sin \varphi - 3\varphi \right) - \frac{B_{1+}}{X^4} \cos \left(\frac{B_{1+}}{X} \sin \varphi - 4\varphi \right) \right] d\theta \\ &\quad - C \int_0^{2\pi} e^{-B_{2+} \cos \varphi / X} (z+h_2) \left[\frac{2}{X^3} \cos \left(\frac{B_{2+}}{X} \sin \varphi - 3\varphi \right) - \frac{B_{2+}}{X^4} \cos \left(\frac{B_{2+}}{X} \sin \varphi - 4\varphi \right) \right] d\theta \\ &\quad + C \int_0^{2\pi} e^{-B_{1-} \cos \varphi / X} (z-h_1) \left[\frac{2}{X^3} \cos \left(\frac{B_{1-}}{X} \sin \varphi - 3\varphi \right) - \frac{B_{1-}}{X^4} \cos \left(\frac{B_{1-}}{X} \sin \varphi - 4\varphi \right) \right] d\theta \\ &\quad - C \int_0^{2\pi} e^{-B_{2-} \cos \varphi / X} (z-h_2) \left[\frac{2}{X^3} \cos \left(\frac{B_{2-}}{X} \sin \varphi - 3\varphi \right) - \frac{B_{2-}}{X^4} \cos \left(\frac{B_{2-}}{X} \sin \varphi - 4\varphi \right) \right] d\theta, \end{aligned} \quad (\text{A9})$$

where

$$B_{1+} = Nt(z+h_1), \quad B_{1-} = Nt|z-h_1|, \quad B_{2+} = Nt(z+h_2), \quad B_{2-} = Nt|z-h_2|.$$

The solution for the perturbation vertical velocity to the surface steady forcing is obtained by integrating (A6) with respect to time:

$$w(x, y, z, t) = \text{Re} \left\{ -C \int_0^{2\pi} \frac{P_+ e^{-P_+}}{(\gamma_+ B)^2} [AP_+^2 - (\gamma_+ + A)P_+ + 2\gamma_+] d\theta \right. \\ \left. + C \int_0^{2\pi} \frac{P_- e^{-P_-}}{(\gamma_- B)^2} [AP_-^2 - (\gamma_- + A)P_- + 2\gamma_-] d\theta \right\}, \quad (\text{A10})$$

where

$$P_+ = \frac{Nt(z+h)}{T}, \quad P_- = \frac{Nt|z-h|}{T}, \quad \gamma_+ = N(z+h), \quad \gamma_- = N|z-h|, \\ B = a_x \sqrt{\cos^2 \theta + \gamma^2 \sin^2 \theta} - i(x \cos \theta + y \sin \theta), \quad \text{and} \quad A = i(U \cos \theta + V \sin \theta).$$

Evaluating the real part of (A10) yields

$$w(x, y, z, t) = C \int_0^{2\pi} \left\{ \frac{B_r^2 - B_i^2}{\gamma_+^2 (B_r^2 + B_i^2)^2} e^{-\gamma_+ t \cos \varphi / X} \left[\left(\frac{\gamma_+ t}{X} \right)^3 (U \cos \theta + V \sin \theta) \sin \left(\frac{\gamma_+ t}{X} \sin \varphi - 3\varphi \right) \right. \right. \\ \left. - \left(\frac{\gamma_+ t}{X} \right)^2 (U \cos \theta + V \sin \theta) \sin \left(\frac{\gamma_+ t}{X} \sin \varphi - 2\varphi \right) \right. \\ \left. + \left(\frac{\gamma_+ t}{X} \right)^2 \gamma_+ \cos \left(\frac{\gamma_+ t}{X} \sin \varphi - 2\varphi \right) \right. \\ \left. - \left(\frac{\gamma_+ t}{X} \right) 2\gamma_+ \cos \left(\frac{\gamma_+ t}{X} \sin \varphi - \varphi \right) \right] \\ + \frac{2B_r B_i}{\gamma_+^2 (B_r^2 + B_i^2)^2} e^{-\gamma_+ t \cos \varphi / X} \left[\left(\frac{\gamma_+ t}{X} \right)^3 (U \cos \theta + V \sin \theta) \cos \left(\frac{\gamma_+ t}{X} \sin \varphi - 3\varphi \right) \right. \\ \left. - \left(\frac{\gamma_+ t}{X} \right)^2 (U \cos \theta + V \sin \theta) \cos \left(\frac{\gamma_+ t}{X} \sin \varphi - 2\varphi \right) \right. \\ \left. - \left(\frac{\gamma_+ t}{X} \right)^2 \gamma_+ \sin \left(\frac{\gamma_+ t}{X} \sin \varphi - 2\varphi \right) \right. \\ \left. + \left(\frac{\gamma_+ t}{X} \right) 2\gamma_+ \sin \left(\frac{\gamma_+ t}{X} \sin \varphi - \varphi \right) \right] \\ - \frac{B_r^2 - B_i^2}{\gamma_-^2 (B_r^2 + B_i^2)^2} e^{-\gamma_- t \cos \varphi / X} \left[\left(\frac{\gamma_- t}{X} \right)^3 (U \cos \theta + V \sin \theta) \sin \left(\frac{\gamma_- t}{X} \sin \varphi - 3\varphi \right) \right. \\ \left. - \left(\frac{\gamma_- t}{X} \right)^2 (U \cos \theta + V \sin \theta) \sin \left(\frac{\gamma_- t}{X} \sin \varphi - 2\varphi \right) \right. \\ \left. + \left(\frac{\gamma_- t}{X} \right)^2 \gamma_- \cos \left(\frac{\gamma_- t}{X} \sin \varphi - 2\varphi \right) \right. \\ \left. - \left(\frac{\gamma_- t}{X} \right) 2\gamma_- \cos \left(\frac{\gamma_- t}{X} \sin \varphi - \varphi \right) \right] \\ - \frac{2B_r B_i}{\gamma_-^2 (B_r^2 + B_i^2)^2} e^{-\gamma_- t \cos \varphi / X} \left[\left(\frac{\gamma_- t}{X} \right)^3 (U \cos \theta + V \sin \theta) \cos \left(\frac{\gamma_- t}{X} \sin \varphi - 3\varphi \right) \right. \\ \left. - \left(\frac{\gamma_- t}{X} \right)^2 (U \cos \theta + V \sin \theta) \cos \left(\frac{\gamma_- t}{X} \sin \varphi - 2\varphi \right) \right. \\ \left. - \left(\frac{\gamma_- t}{X} \right)^2 \gamma_- \sin \left(\frac{\gamma_- t}{X} \sin \varphi - 2\varphi \right) \right. \\ \left. + \left(\frac{\gamma_- t}{X} \right) 2\gamma_- \sin \left(\frac{\gamma_- t}{X} \sin \varphi - \varphi \right) \right] \Big\} d\theta, \quad (\text{A11})$$

where

$$B_r = a_x \sqrt{\cos^2 \theta + \gamma^2 \sin^2 \theta}, \quad \text{and} \quad B_i = x \cos \theta + y \sin \theta.$$

The solution for the perturbation vertical velocity to the finite-depth steady forcing is obtained by integrating (A8) with respect to time or by integrating (A10) with respect to the forcing level:

$$\begin{aligned} w(x, y, z, t) = \text{Re} \left\{ C \int_0^{2\pi} \frac{z + h_1}{(\gamma_{1+} B)^2} [(-AP_{1+}^2 + \gamma_{1+} P_{1+} - \gamma_{1+}) e^{-P_{1+}} + \gamma_{1+}] d\theta \right. \\ - C \int_0^{2\pi} \frac{z + h_2}{(\gamma_{2+} B)^2} [(-AP_{2+}^2 + \gamma_{2+} P_{2+} - \gamma_{2+}) e^{-P_{2+}} + \gamma_{2+}] d\theta \\ + C \int_0^{2\pi} \frac{z - h_1}{(\gamma_{1-} B)^2} [(-AP_{1-}^2 + \gamma_{1-} P_{1-} - \gamma_{1-}) e^{-P_{1-}} + \gamma_{1-}] d\theta \\ \left. - C \int_0^{2\pi} \frac{z - h_2}{(\gamma_{2-} B)^2} [(-AP_{2-}^2 + \gamma_{2-} P_{2-} - \gamma_{2-}) e^{-P_{2-}} + \gamma_{2-}] d\theta \right\}, \end{aligned} \quad (\text{A12})$$

where

$$\begin{aligned} \gamma_{1+} &= N(z + h_1), & \gamma_{1-} &= N|z - h_1|, \\ \gamma_{2+} &= N(z + h_2), & \gamma_{2-} &= N|z - h_2|, \quad \text{and} \end{aligned}$$

$$\begin{aligned} P_{1+} &= \frac{Nt(z + h_1)}{T}, & P_{1-} &= \frac{Nt|z - h_1|}{T}, \\ P_{2+} &= \frac{Nt(z + h_2)}{T}, & P_{2-} &= \frac{Nt|z - h_2|}{T}. \end{aligned}$$

Evaluating the real part of (A12) yields

$$\begin{aligned} w(x, y, z, t) = C \int_0^{2\pi} \left\{ \frac{(z + h_1)(B_r^2 - B_i^2)}{\gamma_{1+}(B_r^2 + B_i^2)^2} e^{-\gamma_{1+} t \cos \phi / X} \left[\frac{\gamma_{1+} t^2}{X^2} (U \cos \theta + V \sin \theta) \sin \left(\frac{\gamma_{1+} t}{X} \sin \phi - 2\phi \right) \right. \right. \\ \left. \left. + \frac{\gamma_{1+} t}{X} \cos \left(\frac{\gamma_{1+} t}{X} \sin \phi - \phi \right) - \cos \left(\frac{\gamma_{1+} t}{X} \sin \phi \right) + 1 \right] \right. \\ + \frac{2(z + h_1)B_r B_i}{\gamma_{1+}(B_r^2 + B_i^2)^2} e^{-\gamma_{1+} t \cos \phi / X} \left[\frac{\gamma_{1+} t^2}{X^2} (U \cos \theta + V \sin \theta) \cos \left(\frac{\gamma_{1+} t}{X} \sin \phi - 2\phi \right) \right. \\ \left. - \frac{\gamma_{1+} t}{X} \sin \left[\frac{\gamma_{1+} t}{X} \sin \phi - \phi \right] + \sin \left(\frac{\gamma_{1+} t}{X} \sin \phi \right) \right] \\ - \frac{(z + h_2)(B_r^2 - B_i^2)}{\gamma_{2+}(B_r^2 + B_i^2)^2} e^{-\gamma_{2+} t \cos \phi / X} \left[\frac{\gamma_{2+} t^2}{X^2} (U \cos \theta + V \sin \theta) \sin \left(\frac{\gamma_{2+} t}{X} \sin \phi - 2\phi \right) \right. \\ \left. + \frac{\gamma_{2+} t}{X} \cos \left(\frac{\gamma_{2+} t}{X} \sin \phi - \phi \right) - \cos \left(\frac{\gamma_{2+} t}{X} \sin \phi \right) + 1 \right] \\ - \frac{2(z + h_2)B_r B_i}{\gamma_{2+}(B_r^2 + B_i^2)^2} e^{-\gamma_{2+} t \cos \phi / X} \left[\frac{\gamma_{2+} t^2}{X^2} (U \cos \theta + V \sin \theta) \cos \left(\frac{\gamma_{2+} t}{X} \sin \phi - 2\phi \right) \right. \\ \left. - \frac{\gamma_{2+} t}{X} \sin \left(\frac{\gamma_{2+} t}{X} \sin \phi - \phi \right) + \sin \left(\frac{\gamma_{2+} t}{X} \sin \phi \right) \right] \\ + \frac{(z - h_1)(B_r^2 - B_i^2)}{\gamma_{1-}(B_r^2 + B_i^2)^2} e^{-\gamma_{1-} t \cos \phi / X} \left[\frac{\gamma_{1-} t^2}{X^2} (U \cos \theta + V \sin \theta) \sin \left(\frac{\gamma_{1-} t}{X} \sin \phi - 2\phi \right) \right. \\ \left. + \frac{\gamma_{1-} t}{X} \cos \left(\frac{\gamma_{1-} t}{X} \sin \phi - \phi \right) - \cos \left(\frac{\gamma_{1-} t}{X} \sin \phi \right) + 1 \right] \\ \left. + \frac{2(z - h_1)B_r B_i}{\gamma_{1-}(B_r^2 + B_i^2)^2} e^{-\gamma_{1-} t \cos \phi / X} \left[\frac{\gamma_{1-} t^2}{X^2} (U \cos \theta + V \sin \theta) \cos \left(\frac{\gamma_{1-} t}{X} \sin \phi - 2\phi \right) \right. \right. \\ \left. \left. - \frac{\gamma_{1-} t}{X} \sin \left(\frac{\gamma_{1-} t}{X} \sin \phi - \phi \right) + \sin \left(\frac{\gamma_{1-} t}{X} \sin \phi \right) \right] \right\} \end{aligned}$$

$$\begin{aligned}
& - \frac{(z - h_2)(B_r^2 - B_i^2)}{\gamma_{2-}(B_r^2 + B_i^2)^2} e^{-\gamma_{2-}t \cos \varphi / X} \left[\frac{\gamma_{2-}t^2}{X^2} (U \cos \theta + V \sin \theta) \sin \left(\frac{\gamma_{2-}t}{X} \sin \varphi - 2\varphi \right) \right. \\
& \quad \left. + \frac{\gamma_{2-}t}{X} \cos \left(\frac{\gamma_{2-}t}{X} \sin \varphi - \varphi \right) - \cos \left(\frac{\gamma_{2-}t}{X} \sin \varphi \right) + 1 \right] \\
& - \frac{2(z - h_2)B_r B_i}{\gamma_{2-}(B_r^2 + B_i^2)^2} e^{-\gamma_{2-}t \cos \varphi / X} \left[\frac{\gamma_{2-}t^2}{X^2} (U \cos \theta + V \sin \theta) \cos \left(\frac{\gamma_{2-}t}{X} \sin \varphi - 2\varphi \right) \right. \\
& \quad \left. - \frac{\gamma_{2-}t}{X} \sin \left(\frac{\gamma_{2-}t}{X} \sin \varphi - \varphi \right) + \sin \left(\frac{\gamma_{2-}t}{X} \sin \varphi \right) \right] \} d\theta. \quad (\text{A13})
\end{aligned}$$

Integrations with respect to θ are performed numerically using an extended trapezoidal rule.

APPENDIX B

Analytic Solution for the Perturbation Vertical Velocity in Two Dimensions

The solution for the perturbation vertical velocity to the finite-depth pulse forcing, which is given by $q(x, z, t) = q_0[a_x^2/(x^2 + a_x^2)]\delta(t)$ for $h_1 \leq z \leq h_2$, in two dimensions is

$$\begin{aligned}
w(x, z, t) = & C' e^{-B_{1+}' \cos \varphi' / X'} \frac{z + h_1}{X'^2} \cos \left(\frac{B_{1+}'}{X'} \sin \varphi' - 2\varphi' \right) \\
& - C' e^{-B_{2+}' \cos \varphi' / X'} \frac{z + h_2}{X'^2} \cos \left(\frac{B_{2+}'}{X'} \sin \varphi' - 2\varphi' \right) \\
& + C' e^{-B_{1-}' \cos \varphi' / X'} \frac{z - h_1}{X'^2} \cos \left(\frac{B_{1-}'}{X'} \sin \varphi' - 2\varphi' \right) \\
& - C' e^{-B_{2-}' \cos \varphi' / X'} \frac{z - h_2}{X'^2} \cos \left(\frac{B_{2-}'}{X'} \sin \varphi' - 2\varphi' \right), \quad (\text{B1})
\end{aligned}$$

where

$$C' = \frac{g a_x q_0}{2 c_p T_0 N}, \quad X' = \sqrt{a_x^2 + (Ut - x)^2},$$

$$\varphi' = \arctan \frac{Ut - x}{a_x}, \quad \text{and}$$

$$\begin{aligned}
B_{1+}' &= Nt(z + h_1), & B_{1-}' &= Nt|z - h_1|, \\
B_{2+}' &= Nt(z + h_2), & B_{2-}' &= Nt|z - h_2|.
\end{aligned}$$

The solution for the perturbation vertical velocity to the finite-depth steady forcing is obtained by integrating (B1) with respect to time. Integration with respect to time is performed numerically using an extended trapezoidal rule.

REFERENCES

- Baik, J.-J., H.-S. Hwang, and H.-Y. Chun, 1999a: Transient critical-level effect for internal gravity waves in a stably stratified shear flow with thermal forcing. *Phys. Fluids*, **11**, 238–240.
- , —, and —, 1999b: Transient, linear dynamics of a stably stratified shear flow with thermal forcing and a critical level. *J. Atmos. Sci.*, **56**, 483–499.
- Bretherton, C., 1988: Group velocity and the linear response of stratified fluids to internal heat or mass sources. *J. Atmos. Sci.*, **45**, 81–93.
- Chun, H.-Y., and J.-J. Baik, 1998: Momentum flux by thermally induced internal gravity waves and its approximation for large-scale models. *J. Atmos. Sci.*, **55**, 3299–3310.
- DeMaria, M., 1985: Linear response of a stratified tropical atmosphere to convective forcing. *J. Atmos. Sci.*, **42**, 1944–1959.
- Hamilton, D. W., Y.-L. Lin, R. P. Weglarz, and M. L. Kaplan, 1998: Jetlet formation from diabatic forcing with applications to the 1994 Palm Sunday tornado outbreak. *Mon. Wea. Rev.*, **126**, 2061–2089.
- Han, J.-Y., and J.-J. Baik, 2008: A theoretical and numerical study of urban heat island-induced circulation and convection. *J. Atmos. Sci.*, **65**, 1859–1877.
- Lin, Y.-L., 1986: Calculation of airflow over an isolated heat source with application to the dynamics of V-shaped clouds. *J. Atmos. Sci.*, **43**, 2736–2751.
- , 1987: Two-dimensional response of a stably stratified shear flow to diabatic heating. *J. Atmos. Sci.*, **44**, 1375–1393.
- , and R. B. Smith, 1986: Transient dynamics of airflow near a local heat source. *J. Atmos. Sci.*, **43**, 40–49.
- , and S. Li, 1988: Three-dimensional response of a shear flow to elevated heating. *J. Atmos. Sci.*, **45**, 2987–3002.
- Mapes, B. E., 1993: Gregarious tropical convection. *J. Atmos. Sci.*, **50**, 2026–2037.
- Olfe, D. B., and R. L. Lee, 1971: Linearized calculations of urban heat island convection effects. *J. Atmos. Sci.*, **28**, 1374–1388.
- Pandya, R., and D. R. Durran, 1996: The influence of convectively generated thermal forcing on the mesoscale circulation around squall lines. *J. Atmos. Sci.*, **53**, 2924–2951.
- Silva Dias, P. L., W. H. Schubert, and M. DeMaria, 1983: Large-scale response of the tropical atmosphere to transient convection. *J. Atmos. Sci.*, **40**, 2689–2707.
- Smith, R. B., 1980: Linear theory of stratified hydrostatic flow past an isolated mountain. *Tellus*, **32**, 348–364.
- , and Y.-L. Lin, 1982: The addition of heat to a stratified airstream with application to the dynamics of orographic rain. *Quart. J. Roy. Meteor. Soc.*, **108**, 353–378.
- Song, I.-S., H.-Y. Chun, R. R. Garcia, and B. A. Boville, 2007: Momentum flux spectrum of convectively forced internal gravity waves and its application to gravity wave drag parameterization. Part II: Impacts in a GCM (WACCM). *J. Atmos. Sci.*, **64**, 2286–2308.
- Stobie, J. G., F. Einaudi, and L. W. Uccellini, 1983: A case study of gravity waves–convective storms interaction: 9 May 1979. *J. Atmos. Sci.*, **40**, 2804–2830.